Design and numerical modelling strategy to form Tailored Fibre Placement preforms: Application to the tetrahedral part with orthotropic final configuration

J. Simon, N. Hamila, C. Binetruy, Sebastien Comas-Cardona, B. Masseteau

Composites: Part A 158 (2022) 106952

Contents lists available at ScienceDirect

Composites Part A

journal homepage: www.elsevier.com/locate/compositesa

Design and numerical modelling strategy to form Tailored Fibre Placement preforms: Application to the tetrahedral part with orthotropic final configuration

J. Simon [a,c,*], N. Hamila [b], C. Binetruy [a], S. Comas-Cardona [a], B. Masseteau [c]

[a] Nantes Université, Ecole Centrale Nantes, CNRS, GeM, UMR 6183, Nantes, F-44000, France
[b] ENI Brest, IRDL, UMR CNRS 6027, F-29200, Brest, France
[c] Nantes Université, IRT Jules Verne, Nantes, F-44000, France

ARTICLE INFO

Keywords:
A. Preform
C. Finite element analysis (FEA)
E. Forming
Tailored Fibre Placement
Modelling

ABSTRACT

Tailored Fibre Placement (TFP) allows manufacturing net shape preforms with continuously varying orientations and thickness. This additive technology, combined with forming, enables the design of fibre reinforced composite parts with optimized fibre orientations. A new modelling strategy to simulate the forming of thin dry TFP preform without backing material is proposed. The finite element model is based on an embedded element formulation, which assumes the stitching yarn to act as a bond between fibre tows of adjacent layers. Fibre tows are modelled with 2-node beam elements having independent generalized stress stiffnesses. The forming of a tetrahedral shape with orthotropic final configuration is addressed both experimentally and numerically to validate the proposed approach. The tetrahedral shape has a direct industrial application since it corresponds to corner brackets. This study also demonstrates the ability to improve the mechanical properties of engineered part using the hybrid TFP-forming process.

1. Introduction

Additive manufacturing of continuous fibre-reinforced composites consists in depositing fibres only where needed (or desired) with the possibility to prescribe curvilinear paths. Continuous Filament Fabrication (CFF) technologies consist in depositing a continuous fibre tow using a specific 3D printer. Filament Winding, Automated Tape Laying, Automated Fibre Placement (AFP), Continuous Tow Shearing (CTS) and Tailored Fibre Placement (TFP) are tow placement technologies which can also be considered as additive manufacturing processes. As AFP, CFF can directly manufacture 3D parts. However, depositing fibres directly on highly double-curved parts without defects can be challenging for these technologies. A two-step approach was recently proposed in [1], where a flat preform is made using CTS before being transformed into a 3D shape via forming. This solution enables lowering cost-production and reducing defects.

A flat TFP preform is made of one or several continuous tows laid down on a flat backing material. Fibres are steered using numerical control to follow prescribed curvilinear paths. The fibre tow remains in place thanks to a zigzag stitching (Fig. 1). TFP offers a large choice of combinations for the backing material, fibre tows and stitching yarn. A single TFP preform can be made of several tow materials and the backing material can be any thin material tolerant to stitching such as a polymer film, a non-woven fabric or a conventional textile. Dry or commingled tow is used depending on the subsequent forming process involved. The stitching yarn material is usually polyester. TFP allows a whole preform to be manufactured or can be used to locally reinforce a conventional textile for instance.

Previous work on TFP focused on aligning fibres with the principal stress directions in 2D parts [2–4]. In particular, the stress concentration in notched plate can be smoothed out by using curvilinear path circumventing the discontinuities [5–8]. Uhlig et al. [9] demonstrate that TFP and Non-Crimp Fabrics (NCF) open-hole laminates have similar strength using cyclic and tensile tests. Continuously varying orientations is a degree of design freedom which allows taking benefit of the intrinsic anisotropy of fibrous reinforcements. However, in case of 3D part manufacturing, the principal stress directions in the part are determined on its 3D final state. The forming process causes a change in fibre orientation and can create defects, especially for complex shaped parts. As a consequence, it is necessary to develop an accurate and efficient model to simulate the forming of TFP preforms which provides information about the final fibre orientation and density. Only few works were dedicated to the manufacturing of 3D parts

* Corresponding author at: Nantes Université, Ecole Centrale Nantes, CNRS, GeM, UMR 6183, Nantes, F-44000, France.
E-mail addresses: jessy.simon@ec-nantes.fr (J. Simon), christophe.binetruy@ec-nantes.fr (C. Binetruy).

https://doi.org/10.1016/j.compositesa.2022.106952
Received 4 February 2022; Received in revised form 28 March 2022; Accepted 2 April 2022
Available online 21 April 2022
1359-835X/

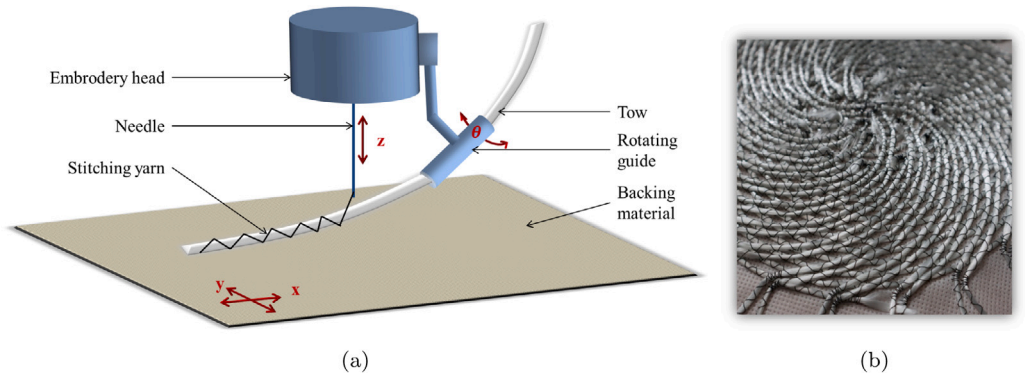

Fig. 1. TFP principle: (a) schematic representation and (b) example of preform.

using TFP. Moreover, they investigated the experimental folding of flat TFP preforms or the influence of cuts in the backing material to avoid formability issues for complex orientations on doubly-curved shapes [10–12]. However, to the best of the authors' knowledge, the numerical modelling of TFP preforms during forming has not been investigated yet.

In this paper, a hybrid solution combining the TFP technology and forming to manufacture highly doubly-curved parts with orthotropic fibre orientations is proposed. A new numerical modelling strategy to simulate the forming of TFP preforms without backing material is proposed for the first time. It aims at demonstrating the advantages of using TFP in 3D composite parts manufacturing and raises the challenges to be addressed to fully exploit the TFP technology in this field.

Various finite element models have been proposed that mainly differ from the scale used to represent the fibrous reinforcement and its behaviour [13–15]. A TFP preform is made of several constituents including the fibre tows, stitching yarn and backing material. In this work, the backing material was removed from the preform prior to forming. The multi-material architecture of TFP preforms inherently makes its modelling complex and time consuming if all the constituents and their interactions are taken into account. Therefore, some assumptions have been made and will be discussed in the remainder of this paper. The TFP modelling strategy proposed herein focuses on tracking the fibre tow orientations and distribution during forming. Since continuously varying orientations can be achieved in a TFP preform, a semi-discrete approach, where fibre tows are represented explicitly using 1D beam elements is developed. The model is based on an embedded element formulation which assumes the stitching yarn to act as a perfect bond between intersecting fibre tows of adjacent layers. The embedded element strategy has already been used to model fibre-reinforced concrete [16–18] or forming of 3D interlocks [19]. In this work, the embedded element approach allow simplifying the interactions such as frictional contact between the constituents of TFP preforms and in particular, avoids developing a realistic but time-consuming modelling of the stitching yarn.

To validate the proposed modelling strategy, experimental and numerical forming on a tetrahedral shape are addressed. This shape has a highly double curvature and corresponds to a corner bracket widely used to design composite structures. This case study will demonstrate the ability of manufacturing 3D orthotropic parts from specifically designed flat TFP preforms which cannot be achieved by forming conventional textiles.

In this paper, Section 2 describes the architecture of TFP preforms and investigates their kinematics during forming through experimental forming on a tetrahedral shape. In Section 3, the objectives and the fundamental hypothesis of the model, required to simplify the complexity of the TFP preform architecture, are presented. The finite element model whose main feature is the use of embedded elements will be described as well as the finite elements implemented to model the different features of the semi-discrete model. Finally, Section 4 presents the forming simulation results of flat TFP preform designed to obtain final composite parts with orthotropic properties. Comparisons with the experimental results of Section 2 are drawn followed by a discussion on the developed TFP preform modelling strategy.

2. TFP preform architecture and deep drawing

2.1. TFP preform deformation mechanisms

As described in Section 1, a TFP preform is made of fibre tows placed on a backing material and remained in place thanks to a zig-zag stitching. Non-Crimp Fabrics (NCF) are conventional textiles whose architecture is most similar to TFP preforms, as they are made of several UD plies stitched together with a through-thickness stitching yarn. TFP preform can be approximately considered as a generalization of NCF to multi-directional plies with the difference that an additional backing material is necessary for the stitching. Besides, this backing material can remain during forming to add polymer matrix or in the case where TFP is used to locally reinforce another conventional textile. In this work, the backing material is removed prior to forming.

During forming, the overall behaviour of a TFP preform will strongly depend on the individual properties of the fibre tows, the stitching yarn, the way they interact with each other as well as the curvilinear path followed by the fibres. Moreover, the stitching parameters, i.e. stitch length, width and tension represented in Fig. 2, strongly influence the behaviour of the TFP preform. The shorter the stitch length, the higher the friction between fibre tows and the stiffer the preform. On one hand, the influence of the stitching parameters over the whole preform behaviour allows varying the stitching parameters inside the preform to overcome forming issues. On the other hand, it increases the architectural complexity of these tailored preforms. Consequently, the behaviour of TFP preforms is inherently complex.

2.2. TFP preform manufacturing

TFP preforms have been manufactured at IRT Jules Verne using the TFP ZSK © CMCW 0200-900D-2500 embroidery machine. A control system for the tension of the upper stitching yarn has been added and the tension of the lower stitching yarn is set via the bobbin's mechanism. The design of the TFP preforms used in the forming experiment was carried out using a Python script that generates the stitch coordinates. This method allows the TFP preform drawing to be set up and the stitch coordinates to be accessed to create the corresponding digital twin.

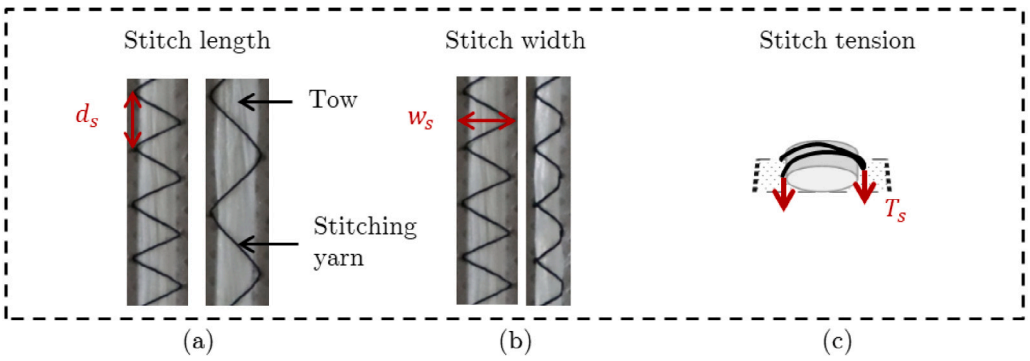

Fig. 2. Stitching process parameters: (a) Stitch length d_s, (b) width w_s and (c) tension T_s.

2.3. Choice of the formed part geometry

To demonstrate the ability of 2-layer TFP preforms to be formed on highly double curved shapes, a tetrahedral shape has been chosen. The tetrahedral shape is a doubly curved shape which corresponds to angle brackets for instance. Therefore, it shows a great interest in industries such as aeronautics. Forming using conventional textiles such as woven fabrics or interlocks on such a shape is possible but requires a specific design of the blank-holders and a control of the pressure applied on them to avoid wrinkles [20–22]. However, if wrinkles can be eliminated from the tetrahedral shape which is the useful part of corner brackets, they cannot be avoided in the flat areas surrounding it [20]. Moreover, the high shear angles (around 60°) weaken the part in those regions. Consequently, forming of tailored 2-layer TFP preform to achieve 0/90° fibre orientations in the final tetrahedral part using basic blank-holders will greatly improve the manufacturing process and the final mechanical properties of the part.

2.4. TFP preforms' materials

The forming experiments are carried out at ambient temperature and require high deformation of the TFP preforms. Rotation between the dry fibre tows of the different layers, known as in-plane shear for conventional textiles, is the main deformation during forming. Consequently, it is difficult to find a backing material able to deform accordingly at room temperature without creating defects. As a result, the backing material has been removed prior to forming. To this end, a PolyVinyl Alcohol (PVA) water soluble film was used as backing material. After manufacturing, the TFP preforms were washed and then dried in an oven at a temperature of 60 °C. The 2690 tex PET/E-glass continuous tow (from P-D-Glasseiden GMBH, Oschatz, Germany) was stitched onto the PVA film (Gunold® Solvy film 80, Stecker) using a 24 tex PET stitching yarn (Serafil fine, Amman). The stitching length and width were set to 2.5 mm and the stitching tension to 5 10^{-2} N. The stitching length is reduced in U-turn and highly curved paths.

2.5. TFP preform forming on a tetrahedral punch with 0/90° final orientations

The forming on a tetrahedral shape aims at demonstrating the ability to achieve 0/90° final orientation in the whole part without defect using a minimalist forming set-up. The 2D displacement field (orthogonal to the punch displacement) and the final angles between the layers on one face of the formed part have been measured for quantitative analysis of the results. Besides, the punch force vs displacement is monitored.

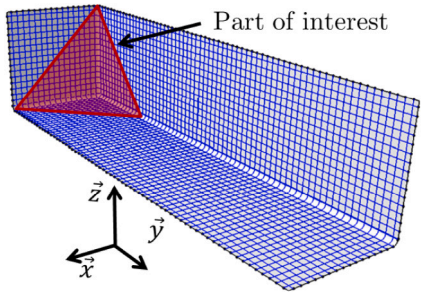

Fig. 3. Example of orthotropic design for a structural part with a triple point.

2.5.1. TFP preform design

Fig. 3 shows an example of structural part having a triple point at the vertex and the desired fibre orientations. Some fibres are parallel to the corner's edges while other are orthogonal to them. As shown in Fig. 4(a), the angle between the edges of one face of the tetrahedral shape is equal to 90°. Their projection in the plane whose normal is parallel to the tetrahedral shape axis gives an angle of 120° (Fig. 4(b)). Consequently, placing fibres parallel to the edges for each face leads to the TFP pattern shown in (Fig. 4(c)) whose fibre orientation will have to change by 30° during forming. Figs. 4(d) and (e) illustrate a possible combination of two layers to obtain the flat pattern presented in Fig. 4(c). Therefore, this design is supposed to lead to the targeted 3D orientation via 30° in-plane shear of the flat TFP preform. Layer 1 is obtained from a spiral equation with points placed every 60° to achieve a hexagonal shape. The number of fibre tows from the centre to the outer edge is equal to 50. Layer 2 is built by offsetting the curve linking the edges of a face for each face with 50 fibre tows. In Fig. 4(d) and (e), the number of tows has been divided by a factor of two for the sake of clarity.

2.5.2. Forming device

The forming device shown in Fig. 5 is composed of a tetrahedral punch mounted on the cross head of a universal testing machine (AG-Xplus by Shimadzu). Two square plates (550 mm × 550 mm × 10 mm) made of poly(methyl methacrylate) were used as blank-holder. One plate is fixed to a metallic frame and the other is placed directly onto the preform. A pin system prevents the movable plate of the blank-holder from moving in the plane. No pressure is applied on the movable plate so that only its weight is distributed on the TFP preform at the contact surface. The punch consists of a tetrahedral part, which is 120 mm high, and a 20 mm thick base. The punch controlled by the testing machine has a stroke of 140 mm with a speed of 15 mm/min.

2.5.3. Optical measurements and post-processing

Quantitative measurements were carried out to compare the results with the forming simulations presented in Section 4. A camera

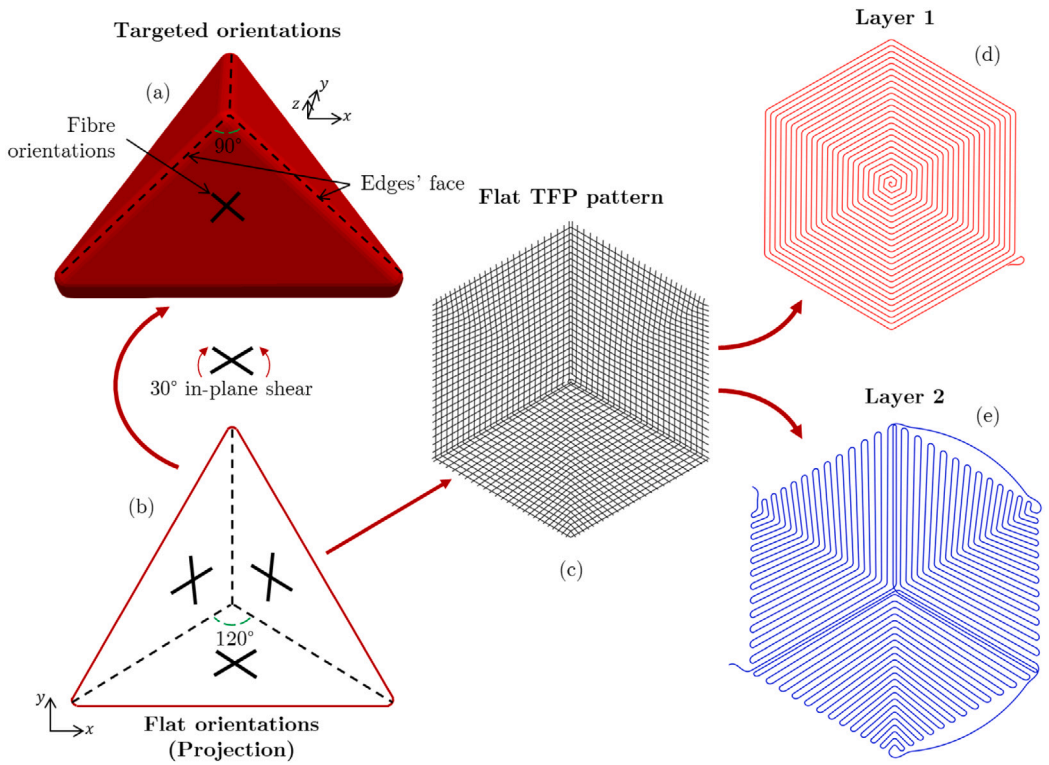

Fig. 4. Design of the TFP preform for the tetrahedral forming: (a) targeted 3D orientations, (b) projection of the 3D orientations along the axis of the tetrahedral shape, (c) flat TFP pattern, (d) first TFP layer and (e) second TFP layer.

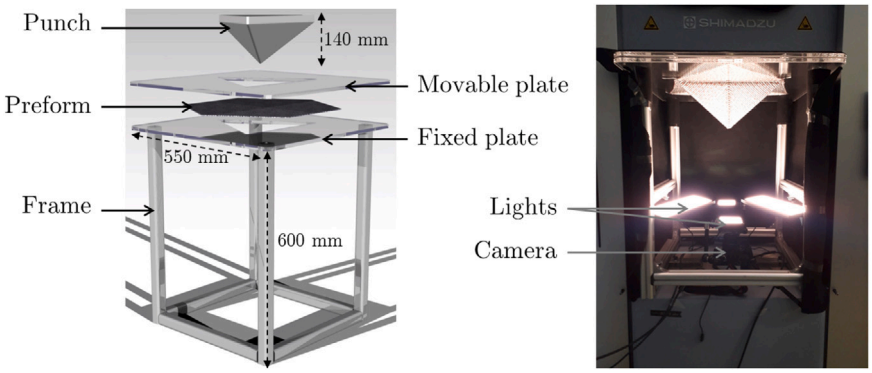

Fig. 5. Tetrahedral forming device: CAO of the forming device (left) and real setup with lights and a camera (left).

positioned along the displacement axis of the punch takes a picture every 2 mm. The camera allows visualizing the 2D displacement field orthogonal to the punch displacement. An EOS Canon Mark II camera was used with a constant focal length of 15 mm and initially set at 520 mm from the TFP preform. At the end of the experiment, a picture was taken after placing the camera according to the normal of one of the face of the tetrahedral punch. This picture allows to measure the final angles between the two layers on one side of the part.

Prior to forming, red-ink markers were drawn on the TFP preform in order to compute the 2D displacement field. The post-processing was achieved using a Python script and the open-source image-processing library OpenCV. Fig. 6 presents the flowchart of the 2D displacement field calculation algorithm. The initialization of the post-processing consists in identifying the markers on the first image (frame 0). From the identified markers, the pixel located at the centre of each marker is stored in the array p_0 which is given as input of a sparse optical flow algorithm. A mesh is built from the triangulation of p_0 for the post-visualization of the 2D field displacement. This algorithm is able to track the motion of a set of pixels from an image to another assuming that intensity variations are negligible between two successive frames and that neighbouring pixels have similar motion. The function "calcOpticalFlowPyrLK" from OpenCV was used and is based on Lucas–Kanade method. The array p_1 represent the position of the pixel p_0 in the ith frame given as second input. Then, the increment of displacement dU is simply computed as the difference between the old (p_0) and the new position (p_1).

2.5.4. Results

Final angle between layers on a face. The final configuration of the TFP preform is shown in Fig. 7. Neither wrinkle nor fibre tow slippage were observed in the formed part.

The angles between the layers on one face have been computed and are shown in Fig. 8. First, the fibre tows were drawn on an open-source software Inkscape and exported into a svg file (Fig. 8(a)). Then, a python script extracts the fibre tows defined as a list of points in the svg file and computes the intersections between the fibre tows of

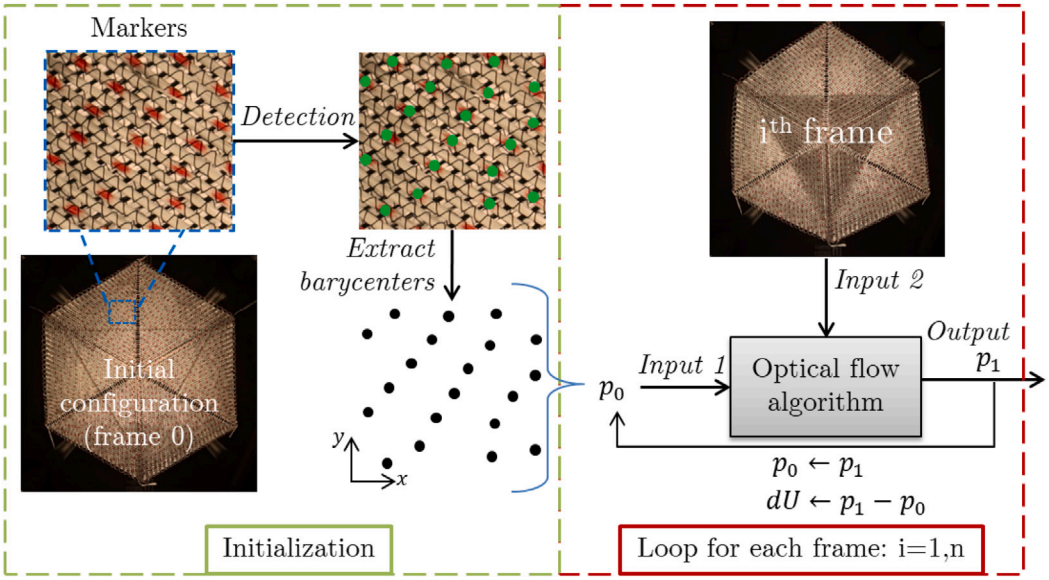

Fig. 6. Flowchart of the post-processing for the computation of the 2D displacement field.

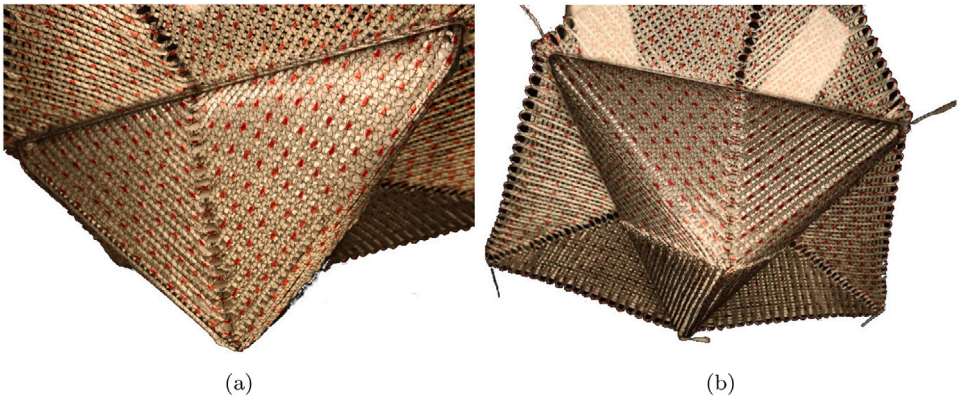

Fig. 7. Final configuration of tetrahedral forming.

the different layers. A mesh is generated from the triangulation of the intersection points and the angles between the layers at the mesh's nodes are computed and displayed (Fig. 8(c)). Fig. 8(b) shows the distribution of angles around 90°. Considering a normal distribution of the angles, a mean angle of 90.72° with a standard deviation of 4.31° is obtained. Due to the chosen design of the layers, the fibres between layers are parallel in the centre of each face. It was noticed too late that this orientation defect can be eliminated by modifying the deposition strategy without impacting the initial orientations in the rest of the preform.

2D displacement field. The result of the marker tracking post-processing to calculate the 2D displacement field is shown in Fig. 9(a). The bottom part of the TFP preform slightly left the camera window during the experiment. Consequently, the markers that are not present during the whole experiment were not processed. This 2D displacement field will be used for comparison with the simulation in the last section of this paper. In particular, this post-processing gives the final contour of the TFP preform which is usually used for comparison with simulation results.

Punch force vs displacement curves. The punch force vs displacement is given in Fig. 9(b). The punch force–displacement has a strong non-linear behaviour. It is composed of a first part from 0 to 120 mm where the punch force increases slowly until the punch stroke reaches the height of the tetrahedral shape (120 mm). Then, the force increases rapidly due to the contact of the TFP preform with the 20 mm thick punch base. The force required during forming is quite low and the movable part of the blank-holder stayed in place. Therefore, the minimal blank-holder setup used is sufficient.

3. Formulation of the TFP preform models

To manufacture flawless 3D parts from TFP preform without trial and error methods, it is necessary to simulate the forming process. This section presents the formulation of the different features of the TFP preform model. First, the objectives to be fulfilled by the modelling strategy are briefly described before choosing the one that is more likely to meet them among the existing ones, i.e. continuum, discrete and semi-discrete modelling strategies. Next, the general principle of the chosen modelling strategy is presented along with its fundamental assumptions. In this study, quasi-static analysis is performed using explicit time integration. Therefore, the finite element formulations are limited to the determination of the internal force vector expression.

3.1. Objectives of the modelling and choice of the strategy

The modelling of TFP preform forming has to provide information on the fibre orientation and distribution in the final 3D part obtained

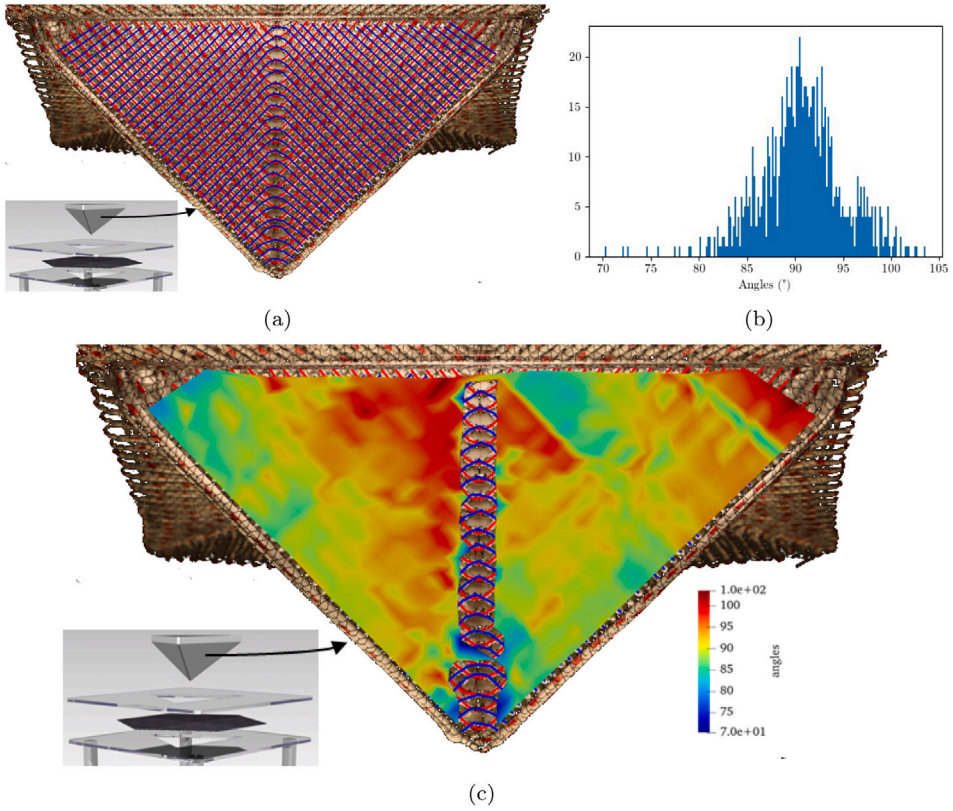

Fig. 8. Angles between layers: (a) curves manually drawn in Inskcape to extract fibre tows, (b) distribution of the angles computed at intersection between fibre tows and (c) angles between the layers at the mesh's nodes.

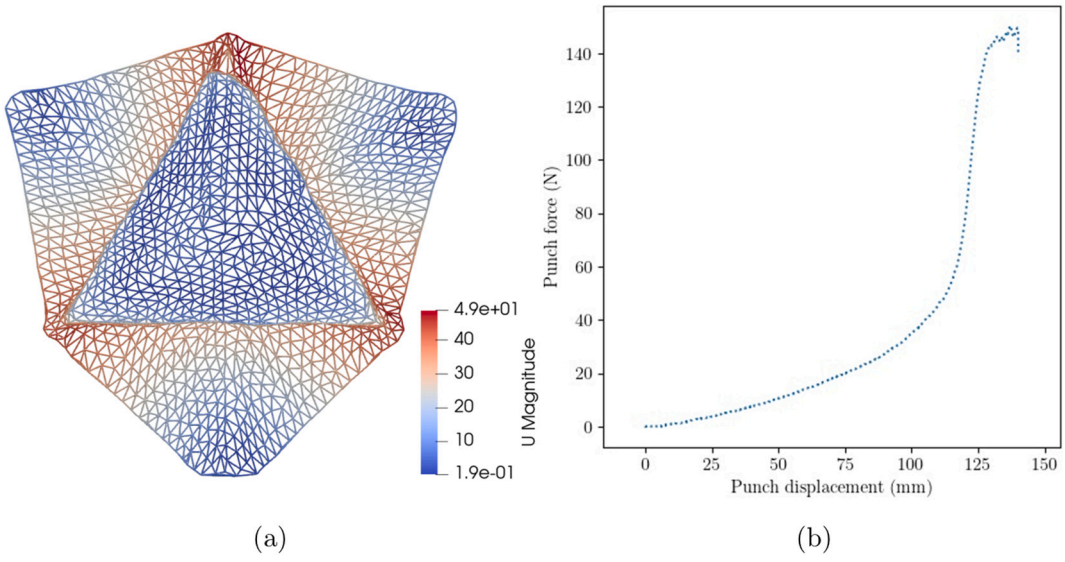

Fig. 9. (a) 2D displacement field (mm): last frame and superimposed wireframe mesh displaying 2D displacement magnitude, (b) Punch force–displacement curve for the tetrahedral forming experiment.

after forming. Besides, the occurrence of defects must also be predicted, such as wrinkles observed in conventional textile forming.

TFP inherently offers a high degree of freedom for the design of tailored preforms. Therefore, the model must allow for all the capabilities of TFP, such as curvilinear fibre placement and heterogeneity of the fibre tow distribution. With this philosophy in mind, a semi-discrete model where fibre tows are modelled explicitly using 1D elements was considered more appropriate than using a continuum approach requiring robust homogenization procedures. The modelling of the stitching yarn is reduced to the minimal for the sake of efficiency. Obviously, other modelling strategies are possible. However, as a first contribution to the simulation of TFP preform forming, this approach was deemed a good compromise between model accuracy and simplicity of development.

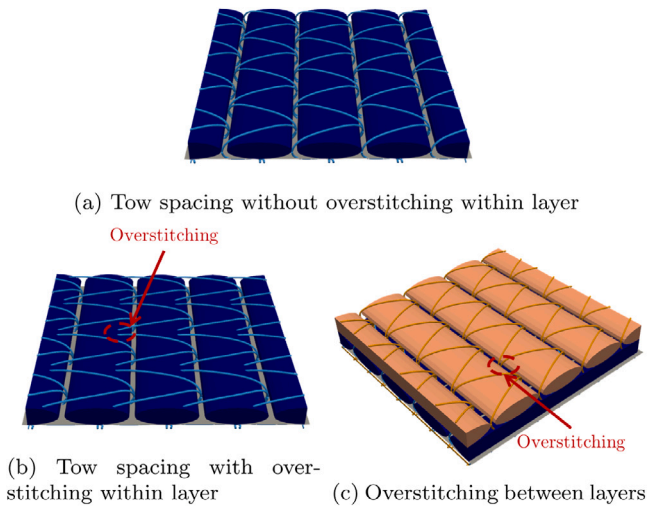

Fig. 10. Influence of the overstitching on the cohesion between fibre tows.

3.2. Semi-discrete modelling and fundamental hypothesis

The first step is to distinguish between weak and strong deformation modes and interactions. To this end, the elementary behaviour and the role of each component of the TFP preform are first described.

3.2.1. Fibre tows

Fibre tows are the main component of a TFP preform that constitutes the core of the reinforcement. Continuous fibre tows have predominant axial stiffness and a generally low bending stiffness. However, as mentioned in [23], the bending stiffness strongly influences the shape of wrinkles and is therefore required for a good prediction of this forming defect.

3.2.2. Stitching yarn

The stitching yarn allows the fibre tows to be precisely placed and maintained on the backing material during the manufacturing of the flat preform. It is responsible for the cohesion between the fibre tows and the backing material, as well as between the fibre tows within the same layer or between adjacent layers. The stitching parameters, i.e. the length, width and tension of the stitches, as well as the spacing of fibre tows, directly influence this cohesion. As shown in Fig. 10, overstitching within a layer or between layers increases the cohesion of the TFP preform. The stitching yarn material can be a polymer that can be melted during forming. In this case, it can be very complex to control and predict the motion of the fibre tows. As noticed in the forming experiments, the stitching yarn ensures a strong cohesion between the layers, even after removing the backing material, due to overstitching between layers.

3.2.3. Fundamental hypothesis of the modelling

Continuously varying orientations is the main feature of TFP preforms. Therefore, it was chosen to explicitly model the fibre tows using 1D finite elements to track these orientations during forming. Beam elements are required to take into account the axial and bending stiffness of fibre tows. Fibre tows of the next layer lie on top of the fibre tows of a previous layer and remain there thanks to the stitching yarn. The stitching yarn is the constituent most likely to be difficult to model. In NCF, it has been shown that the stitching yarn has a strong influence on the shear behaviour [24,25]. When stacking several layers in TFP preforms, the stitching yarn over-stitches the tows of the previous layers. Consequently, considering the fibre tows of the next layer as being fixed on those of the previous layer seems to be a reasonable assumption. In other words, it is considered that the stitching yarn acts as a bond between intersecting fibre tows of adjacent layers. This means that slippage between the fibre tows of different layers is neglected. Therefore, the stitching yarn is not modelled explicitly but involves a transfer of forces between the fibre that cross each other in the adjacent layers. For the case where the stitching yarn is melted, it would be necessary to model the contacts between all the fibre tows, which would be very expensive. In addition, the preform cohesion would be very low and could lead to many defects in the case of complex parts. Therefore, it is assumed that the stitching yarn remains and ensures the preform cohesion during forming.

Although fibre tows between layers exhibit interactions due to friction and overstitching, it is not realistic to consider them as perfectly bound to each other. The rotation of intersecting fibre tows, known as in-plane shear in conventional textiles, is not free. For simplicity, a linear elastic torsional spring is added to each fibre tow intersection, which only takes into account the frictional resistance as well as the stitching yarn deformation due to the rotation of the crossing fibre tows.

3.3. TFP preform model representation

Finally, the fibre tows are modelled using beam elements. The stitching yarn is modelled implicitly by embedding the fibre tows of the next layer in the fibre tows of the previous layer. In the following, the beam element used to model the fibre tows is formulated. Next, the formulation of the embedding constraint modelling the action of the stitching yarn is detailed. Fig. 11 illustrates the definition of the model from a 3D representation of two intersecting fibre tows using the open-source software Texgen. In this figure, a virtual offset is used for clarity only, which means that fibre tows are connected at their neutral axis in the model.

3.4. Fibre tow modelling: Formulation of a beam element

Fibre tows are modelled with beam elements to take into account the different deformation modes and not only the high tensile stiffness. A 2-node flexible shear beam element, which has been widely studied [26–28], is formulated. Therefore, the major key points are presented and references for further computation details are given.

3.4.1. Assumptions

In this formulation, the cross sections of the beam remain plane and do not deform during elastic deformations. Strains are small and finite rotations are allowed.

3.4.2. Kinematics

The beam element has two nodes and each of them has three displacement degrees of freedom (dofs) and three rotation dofs. The position of a point in the initial and current configurations is defined as:

$$\vec{X} = S\vec{E}_1 + X_2\vec{E}_2 + X_3\vec{E}_3 \quad \text{(Initial)} \tag{1}$$

$$\vec{x} = \vec{\phi_0}(S) + X_2\vec{e}_2 + X_3\vec{e}_3 \quad \text{(Current)} \tag{2}$$

S is the curvilinear abscissa of the beam axis in the initial configuration and (X_2, X_3) are the coordinates of the cross section plane. As the cross section does not deform (no warping), the plane coordinates (X_2, X_3) are unchanged in the deformed configuration. ϕ_0 corresponds to the position of a point located on the neutral axis. $\boldsymbol{E}$ and $\boldsymbol{e}$ define respectively the initial and current orientations of the cross section (Fig. 12). Since transverse shear is allowed, the tangent vector to the centroid line $\vec{g}_1$ might be different from the cross section normal $\vec{e}_1$.

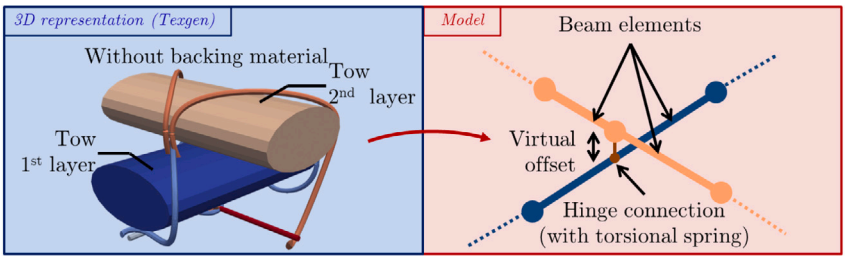

Fig. 11. TFP preform model.

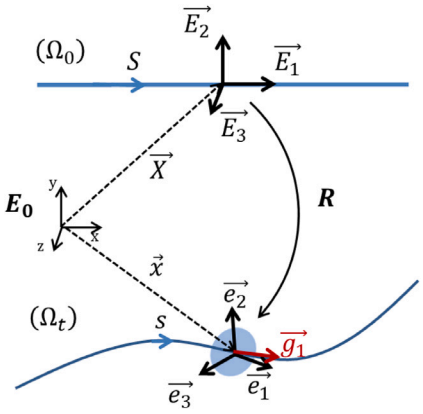

Fig. 12. Initial (Ω_0) and current (Ω_t) beam configurations.

3.4.3. Finite rotation parameterization

The current orientation of the cross section $\boldsymbol{e}$ results from applying the rotation operator $\boldsymbol{R}(\vec{\psi})$ to the initial orientation cross section $\boldsymbol{E}$ (Eq. (3)). The Cartesian rotation pseudo-vector $\vec{\psi} = \psi\vec{n}$ where ψ is the rotation amplitude and $\vec{n}$ is the rotation axis, is used and computed from the rotational degrees of freedom of the beam.

$$\boldsymbol{e} = \boldsymbol{R}\boldsymbol{E} \tag{3}$$

In addition to the rotation operator $\boldsymbol{R}$, the tangent rotation operator $\boldsymbol{T}$ and its vector derivative $\boldsymbol{T}' = DT\left[\frac{d\vec{\psi}}{dS}\right]$ are required. $\boldsymbol{R}$, $\boldsymbol{T}$ and $\boldsymbol{T}'$ are computed using the family of trigonometric functions established in [28].

3.4.4. Strain and curvature vectors

Strains and curvatures are computed from the displacement gradient, more precisely through the difference between the deformation position gradient in the current and initial configurations brought back to the material frame:

$$\begin{aligned}\vec{D}\left(S, X_2, X_3\right) &= \boldsymbol{R}^T\frac{d\vec{x}}{dS} - \frac{d\vec{X}}{dS}\\ &= \boldsymbol{R}^T\left(\frac{d\vec{\phi}_0}{dS} - \vec{e}_1\right) + \boldsymbol{R}^T\frac{d\boldsymbol{R}}{dS}\left(X_2\vec{e}_2 + X_3\vec{e}_3\right)\end{aligned} \tag{4}$$

From this expression, the strain and curvature vectors are identified.

$$\vec{\Gamma} = \boldsymbol{R}^T\left(\frac{d\vec{\phi}_0}{dS} - \vec{e}_1\right) \qquad \vec{K} = \mathrm{vec}\left(\boldsymbol{R}^T\frac{d\boldsymbol{R}}{dS}\right) = \boldsymbol{T}^T\frac{d\vec{\psi}}{dS} \tag{5}$$
$$= \begin{bmatrix} E \\ \Gamma_1 \\ \Gamma_2 \end{bmatrix} \qquad = \begin{bmatrix} K_T \\ K_1 \\ K_2 \end{bmatrix}$$

In Eq. (5), E is the longitudinal strain component, Γ_1 and Γ_2 are the transverse shear components. The matrix $\tilde{\boldsymbol{K}} = \boldsymbol{R}^T\frac{d\boldsymbol{R}}{dS}$ is the skew symmetric matrix of the curvature vector $\vec{K}$. K_T is the torsional strain of the neutral axis whereas K_1 and K_2 are the bending strains along the cross section axis.

3.4.5. Equilibrium equations, internal virtual work and strain-curvature variations

The quasi-static equilibrium equations in the material frame are given hereafter for both forces (Eq. (6)) and moments (Eq. (7)):

$$\frac{d\vec{F}}{dS} + \tilde{K}\vec{F} + \boldsymbol{R}^T\vec{f}_{\vec{p}} = \vec{0} \tag{6}$$

$$\frac{d\vec{M}}{dS} + \left(\boldsymbol{R}^T\frac{d\vec{\phi}_0}{dS}\right)\times\vec{F} + \tilde{\boldsymbol{K}}\vec{M} + \boldsymbol{R}^T\vec{m}_{\vec{p}} = \vec{0} \tag{7}$$

$\vec{F} = \begin{bmatrix} N & Q_1 & Q_2 \end{bmatrix}^T$ and $\vec{M} = \begin{bmatrix} M_T & M_1 & M_2 \end{bmatrix}^T$ are respectively the force and moment vectors in the material frame. N is the tensile force, Q_1 and Q_2 are the transverse shear forces of the cross section. M_T is the torsional moment, M_1 and M_2 are the bending moments. $\vec{f}_{\vec{p}}$ and $\vec{m}_{\vec{p}}$ are external distributed forces and moments in the spatial frame brought back to the material frame by applying $\boldsymbol{R}^T$.

Using the weak form of the equilibrium equations in the material frame, the internal virtual work can be expressed as:

$$\delta W_{int} = \int_0^L \left(\vec{F}\delta\vec{\Gamma} + \vec{M}\delta\vec{K}\right)dS \tag{8}$$

where L is the initial length of the beam.

To compute the internal forces, expressions for the strain and curvature variations are required. They can be derived by differentiating the expressions for the strain and curvature vectors given in Eq. (5):

$$\begin{bmatrix}\delta\vec{\Gamma}\\ \delta\vec{K}\end{bmatrix} = \underbrace{\begin{bmatrix}\boldsymbol{R}^T & 0 & \widetilde{\boldsymbol{R}^T\vec{\phi}_0{}'\boldsymbol{T}^T}\\ 0 & \boldsymbol{T}^T & \tilde{\boldsymbol{K}}\boldsymbol{T}^T + \boldsymbol{T}'\end{bmatrix}}_{\boldsymbol{D}}\begin{bmatrix}\delta\vec{\phi}_0{}'\\ \delta\vec{\psi}'\\ \delta\vec{\psi}\end{bmatrix} \tag{9}$$

Then, the relationship between the variations of $\left(\vec{\phi}_0{}', \vec{\psi}', \vec{\psi}\right)$ and the variations of the nodal parameters can be expressed using the interpolation shape function of the beam. In this study, a linear interpolation is performed leading to Eq. (10).

$$\begin{bmatrix}\delta\vec{\phi}_0{}'\\ \delta\vec{\psi}'\\ \delta\vec{\psi}\end{bmatrix} = \underbrace{\begin{bmatrix}N_1'\boldsymbol{I} & \boldsymbol{0} & N_2'\boldsymbol{I} & \boldsymbol{0}\\ \boldsymbol{0} & N_1'\boldsymbol{I} & \boldsymbol{0} & N_2'\boldsymbol{I}\\ \boldsymbol{0} & N_1\boldsymbol{I} & \boldsymbol{0} & N_2\boldsymbol{I}\end{bmatrix}}_{\boldsymbol{Q}}\begin{bmatrix}\delta\vec{\phi}_{01}\\ \delta\vec{\psi}_1\\ \delta\vec{\phi}_{02}\\ \delta\vec{\psi}_2\end{bmatrix} \tag{10}$$

Combining Eqs. (9) and (10), the strain–displacement matrix $\boldsymbol{B}$ is obtained:

$$\boldsymbol{B} = \boldsymbol{D}\boldsymbol{Q} \tag{11}$$

Then, the expression of the internal forces vector can be deduced:

$$\vec{F_{int}} = \int_0^L \boldsymbol{B}^T\begin{bmatrix}\vec{F}\\ \vec{M}\end{bmatrix}dS \tag{12}$$

3.4.6. Constitutive law

The forces and moments vectors are related to the strains and curvatures vectors by the following equation:

$$\begin{bmatrix} \vec{F} \\ \vec{M} \end{bmatrix} = \boldsymbol{C} \begin{bmatrix} \vec{\Gamma} \\ \vec{K} \end{bmatrix} \tag{13}$$

As a tow is not a continuum, independent section stiffness are used. Moreover, couplings between the deformation modes are neglected. Therefore, the constitutive matrix $\boldsymbol{C}$ is a diagonal matrix given by:

$$\boldsymbol{C} = \text{diag}\begin{pmatrix} C_E & C_{\Gamma 1} & C_{\Gamma 2} & C_{K1} & C_{K2} & C_{K3} \end{pmatrix}$$

C_E is the tensile stiffness, $C_{\Gamma 1}$ and $C_{\Gamma 2}$ are the transverse shear stiffnesses. C_{K1} is the torsional stiffness, C_{K2} and C_{K3} are the bending stiffnesses.

3.5. Stitching yarn modelling: Formulation of the embedding constraint

3.5.1. Embedded element approach: general definition

The embedded element approach consists in embedding elements into other elements of higher dimension called host elements. The embed of 1D elements into 2D elements and 3D elements has been used in reinforced concrete simulations [16–18]. De Luycker et al. [19] embedded 1D elements into 3D elements to model the forming of 3D interlocks. The embed of a 2D membrane into a 3D solid is also a possible option. The embedding constraint means that the kinematic variables, i.e. displacement, velocity and acceleration, at embedded nodes are computed from those defined at the host nodes. Therefore, there is no relative movement between a host element and the elements it embeds.

The embedded element approach generalized the strategy developed in [29,30] where 1D elements are placed either on the edges or on the diagonals of the 2D elements, which in both cases means that the nodes of the embedded element are located on the nodes of the host elements. In the general case, the nodes of the embedded element can be placed anywhere on the host element. However, an embedded element cannot cross the boundaries of a host element, which means that all the nodes of the embedded element are located either inside or on the edges of the same host element.

In the TFP preform model, at each crossing of fibre tows, a node is required in the mesh of the next layer (embedded layer). This node, considered as a 0D element, is embedded in the 1D element of the previous layer (host layer). The embedding of the next layer into the previous layer allows for an independent meshing of both layers, except for some nodes in the embedded layer that are needed at the intersections with the host layer. Since the TFP constituents are supposed to lie on the same plane in the flat configuration, this model might only be valid for thin preforms.

3.5.2. Finite element model generation

Once the host layer has been meshed, the embedded layer is meshed independently, except for some nodes that are required at the intersections between the fibre tows of the host layer and those of the embedded layer.

For each embedded node, the natural coordinates (ξ_e) in the host element are computed by solving Eq. (14) using the Newton–Raphson method:

$$\|\vec{x^e} - \sum_i N_i^h(\xi_e)\,\vec{x_i^h}\| = 0 \tag{14}$$

where $\vec{x^e}$ is the position of the embedded node and (ξ_e) are the natural coordinates of this node in the host element. N_i^h and $\vec{x_i^h}$ are respectively the shape function and the position of the ith node of the host element.

3.5.3. Embedded formulation

Kinematics. The embed of a node into a host element is achieved by computing the position of embedded node from the position of the nodes of the host element:

$$\vec{x^e} = \sum_i N_i^h(\xi_e)\,\vec{x_i^h} \tag{15}$$

In this model, only the displacement degrees of freedom of the embedded node of a beam are driven by the host beam element. In fact, adding the embed of the rotational degrees of freedom would weld the beams together. As mentioned earlier, the resistance to rotation between intersecting fibre tows is taken into account through a linear elastic torsional spring.

Internal forces contribution. As a consequence of this kinematic constraint, the internal forces of an embedded node are transferred to the nodes of the host element. Therefore, the internal forces of a host element at node α are composed of the internal forces $F^{\alpha}_{int_b}$ resulting from the host element behaviour and the internal forces $F^{\alpha}_{int_e}$ due to the embedded nodes (Eq. (16)):

$$F^{\alpha}_{int} = F^{\alpha}_{int_b} + F^{\alpha}_{int_e} \tag{16}$$

The internal forces due to the embedded nodes are computed from the internal forces F^k_{int} at the k-nodes which are embedded, as given by Eq. (17):

$$F^{\alpha}_{int_e} = \sum_k N_{\alpha}(\xi_k) F^k_{int} \tag{17}$$

Fig. 13 illustrates the transmission of the internal forces from one embedded node k_1 to a host element. The red and solid arrows correspond to the internal forces of the embedded node which are transmitted to the host element. The green arrows correspond to the contribution from the embedded node and adds up to the internal forces of the host element (light blue arrows) to form the total internal forces at the host nodes (dark blue arrows).

Mass contribution. Regarding the computation of the mass matrix, the contribution of the embedded nodes to a host element is computed according to Eq. (18) established in [31].

$$M^{\alpha\beta} = \sum_k N_{\alpha}(\xi_k) M^k N_{\beta}(\xi_k) \tag{18}$$

In Eq. (18), Greek superscript refers to the nodes of the host element, whereas Latin superscript refers to the embedded nodes. As explicit time integration is performed in the present study, a lumped mass matrix is used. Therefore, M^k is the lumped mass of the kth embedded node. Although lumping the mass matrix in the presence of embedded elements is not straightforward, it is done by summing the columns of the mass matrix (sum over β index). In the case of quasi-static analyses, this approximation is supposed to have minor effects on the results.

Fig. 14 describes the general workflow of an explicit finite element solver under embedding constraints.

4. Simulation of TFP preform forming

This section investigates the validity of the proposed TFP preform model through forming simulation on the tetrahedral shape. The 2D displacement field and the angles between layers on one face are compared with the measurements shown in the previous section. Finally, the major results of this study are discussed as well as future challenges.

4.1. General settings

4.1.1. Material parameters

The TFP preform model depends on seven material parameters. The beam element required six material parameters, namely, the tensile stiffness (C_E), the transverse shear stiffnesses ($C_{\Gamma 1}, C_{\Gamma 2}$), the torsional

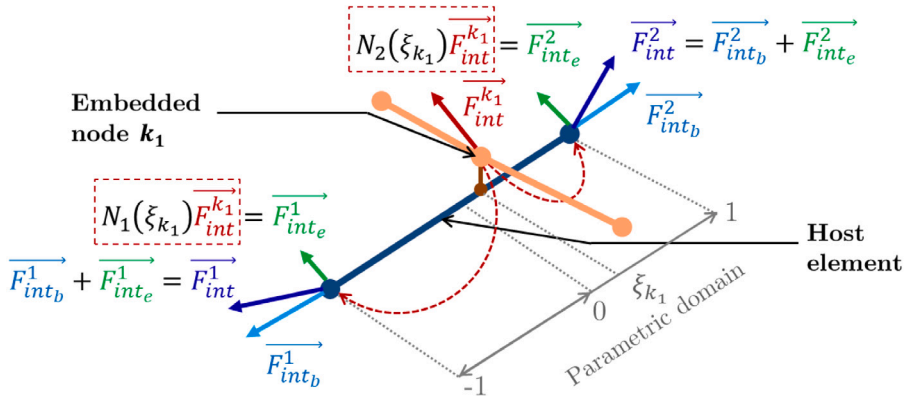

Fig. 13. Transmission of the internal forces from embedded nodes to the embedding element.

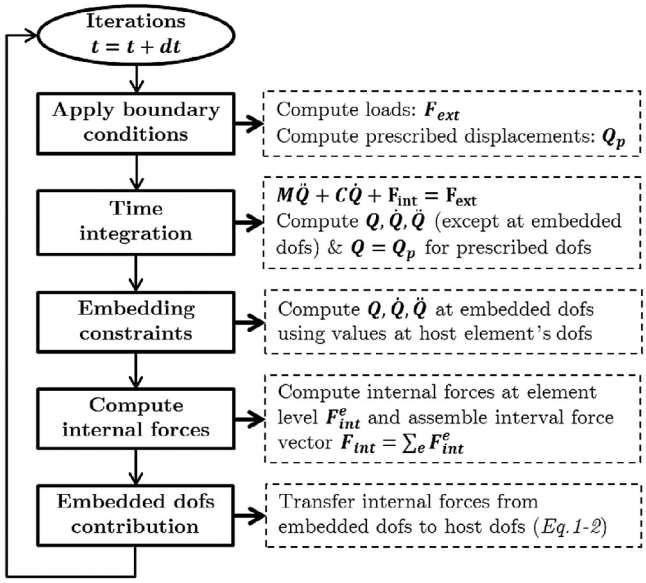

Fig. 14. Flowchart for an explicit finite element solver including embedding constraints.

Table 1
Material parameters for the simulation.

Element	Parameter	Value	Unit
Beam	C_E	1400	kN
	$C_{\Gamma 1}$	700	kN
	$C_{\Gamma 2}$	700	kN
	C_{K1}	1	kN mm^2
	C_{K2}	0.1	kN mm^2
	C_{K3}	1	kN mm^2
Torsional spring	C_{T_s}	1	N mm

stiffness (C_{K1}) and the bending stiffnesses (C_{K2}, C_{K3}). Besides, the linear coefficient of the torsional springs at intersections between fibre tows of different layers is C_{T_s}. Due to a lack of resources, the characterization of these material parameters has not been carried out. Consequently, the values of the material parameters given in Table 1 have been estimated and are supposed to give an acceptable order of magnitude. In particular, the tensile stiffness C_E is estimated from the Young's modulus of E-glass fibres taken equal to 72.5 GPa. The value of the transverse shear stiffness is taken as half the value of the axial stiffness. The torsional and bending stiffness have non zero but low values.

4.1.2. Finite element solver

A research finite element code based on explicit time integration scheme has been developed especially for this study. The contact interactions between the forming tools (blank-holders, punch) and the TFP preforms are solved using the forward increment Lagrangian multipliers method [32]. Forming tools are modelled using discrete rigid surfaces. A constant time step of 10^{-4} s is used for the simulations.

4.2. Tetrahedral shape forming

4.2.1. Finite element model

Layer 1 is first meshed with an element size of 2.5 mm. Then, layer 2 is meshed with the same element size and nodes are appended at intersections with the first layer. These additional nodes are embedded in the corresponding host elements of layer 1. The adjacent nodes of the nodes located at the intersections are deleted if the element size is lower than half the initially prescribed size. The total number of beam elements is 22190 and the simulation runs in 12 h using four cores of an Intel(R) Core(TM) i7-8750H CPU 2.20 GHz processor. The friction coefficient between the fibre tows and the forming tools is equal to 0.2, even though it might be different since the blank-holders are made of PMMA and the punch of PLA. A displacement of 140 mm is imposed to the punch. Regarding the blank-holder, the fixed part is clamped and the movable part can only move along the punch axis.

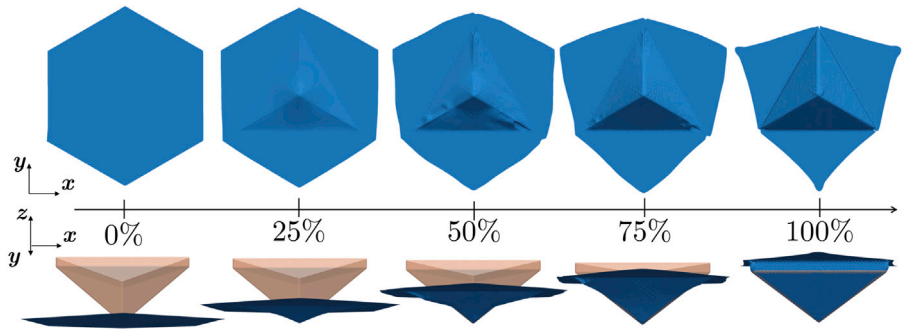

Fig. 15. Top and side views of the tetrahedral shape forming simulation at different instants.

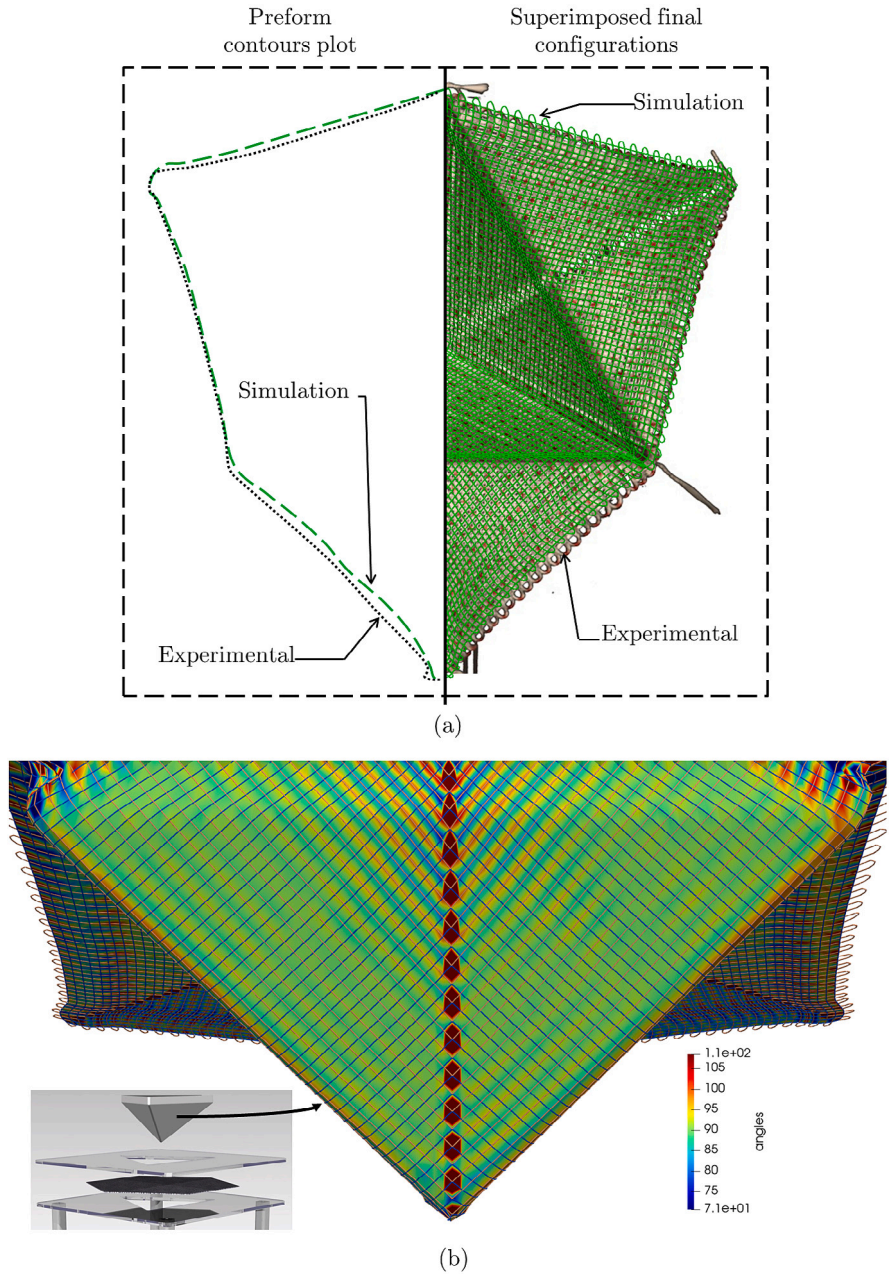

Fig. 16. (a) Comparison between experimental and numerical results: experimental preform contour (dotted line) and simulation (dashed line) (left) and superposition of the final configurations of experimental (picture) and simulation (green wireframe mesh) (right), (b) Final angles between layers on one face: the surface displaying the smooth angle field was built by triangulation of the intersections between the fibre tows.

4.2.2. Results and comparison with experiments

Fig. 15 shows the configuration of the TFP preform at different times from top and side views. In Fig. 16(a), the final configuration of the simulation is superimposed on the experimental result. The predicted contour matches well the experimental one. In the TFP path of the simulation, the curved paths connecting the straight ones have been removed for simplicity. It might contribute to the differences observed between the contours.

Fig. 16(b) shows the final angles between the two layers on a face of the tetrahedral shape. The angles are very close to 90° at every position on the face.

4.3. Discussions and extension of the proposed modelling strategy

As a first attempt, the proposed TFP preform model is quite efficient and gave satisfactory results. The numerical tool developed in this work aims at helping the mechanical designer to predict the formability of flat TFP preforms.

However, to improve the prediction of this model when the fibre tows density in the layers is higher, the lateral contact between the fibre tows has to be taken into account. This could be achieved by adding contact interactions between the beam elements. Moreover, the stitching yarn, which was supposed to act as a hinge connection between intersecting fibre tows, could be modelled differently to take into account slippage between fibre tows. The linear elastic torsional springs at intersections could also be modified to account for non-linear behaviour.

The modelling strategy proposed in this paper allows the modelling of TFP preforms without backing material. However, it would also be interesting to investigate the forming of preforms made from conventional textiles that are locally reinforced with TFP. For instance, continuous tows can be added in some regions to remove stress concentration, especially around holes. Stitching a continuous tow on top of conventional textiles will modify their behaviour during forming and could lead to defects. Consequently, extending the proposed work to TFP preforms with backing material is a challenge to be addressed.

In the example addressed in this work, the determination of the flat TFP pattern leading to an orthotropic configuration in the final 3D parts was achieved intuitively. To address the orthotropic design of parts with even more complex geometries, a numerical method performing the "flattening" of the 3D orthotropic design needs to be developed. An interesting approach has been proposed in [1] which is based on the reverse numerical modelling of double diaphragm forming and was applied to a single layer CTS preform.

5. Conclusions

The forming of dry and thin TFP preforms without backing material has been investigated both experimentally and numerically on a tetrahedral shape. It was shown that an orthotropic final configuration ($90.72° \pm 4.31$), which cannot be achieved using conventional textiles, can be obtained with TFP preforms. The tetrahedral shape has a direct industrial application since it corresponds to corner brackets. Therefore, this work demonstrates the ability to improve the mechanical properties of structural part using TFP preform forming.

A finite element model of TFP preforms is proposed and based on an embedded element formulation where the stitching yarn acts as a bond between intersecting fibre tows of adjacent layers. The fibre tows are modelled using beam elements with independent generalized stress stiffnesses. The fibre tows of the next layer are embedded in the tows of the previous layer. The model assumes quasi-inextensibility of the fibre tows and no slip between the components of the TFP preform. The forming simulations of the tetrahedral shape gave results in good agreement with the experimental ones. Lateral contact between fibre tows of the same layer and slippage between tows of adjacent layers could be incorporated in case of higher fibre density preforms.

Finding a suitable backing material that allows for very large deformations and stitching is difficult. In future works, modelling the forming of TFP preforms with backing material should be investigated. This model could take into account tow-to-backing material slippage, while keeping an embedded element formulation. This new model will allow simulating the forming of TFP preforms with conventional textiles as backing material and therefore addressed another application of the TFP technology, namely local reinforcement.

CRediT authorship contribution statement

J. Simon: Conceptualization, Methodology, Investigation, Writing – original draft. **N. Hamila:** Supervision, Methodology, Writing – review & editing. **C. Binetruy:** Supervision, Methodology, Writing – review & editing. **S. Comas-Cardona:** Supervision, Methodology, Writing – review & editing. **B. Masseteau:** Resources.

Declaration of competing interest

The authors declare that they have no known competing financial interests or personal relationships that could have appeared to influence the work reported in this paper.

Acknowledgement

This work was funded by IRT Jules Verne as part of the Ph.D program PERFORM.

References

[1] Sun X, Belnoue JP-H, Wang W-T, Kim BC, Hallett SR. "Un-forming" fibre-steered preforms: Towards fast and reliable production of complex composites parts. Compos Sci Technol 2021;216:109060.
[2] Spickenheuer A, Schulz M, Gliesche K, Heinrich G. Using tailored fibre placement technology for stress adapted design of composite structures. Plastics, Rubber Compos 2008;37(5):227–32.
[3] Uhlig K, Spickenheuer A, Bittrich L, Heinrich G. Development of a highly stressed bladed rotor made of a CFRP using the tailored fiber placement technology. Mech Compos Mater 2013;49(2):201–10.
[4] Katagiri K, Honda S, Nakaya S, Kimura T, Yamaguchi S, Sonomura H, et al. Tensile strength of CFRP with curvilinearly arranged carbon fiber along the principal stress direction fabricated by the electrodeposition resin molding. Composites A 2021;143:106271.
[5] Crothers P, Drechsler K, Feltin D, Herszberg I, Kruckenberg T. Tailored fibre placement to minimise stress concentrations. Composites A 1997;28(7):619–25.
[6] Gliesche K. Application of the tailored fibre placement (TFP) process for a local reinforcement on an "open-hole" tension plate from carbon/epoxy laminates. Compos Sci Technol 2003;63(1):81–8.
[7] Koricho EG, Khomenko A, Fristedt T, Haq M. Innovative tailored fiber placement technique for enhanced damage resistance in notched composite laminate. Compos Struct 2015;120:378–85.
[8] El-Dessouky HM, Saleh MN, Gautam M, Han G, Scaife RJ, Potluri P. Tailored fibre placement of commingled carbon-thermoplastic fibres for notch-insensitive composites. Compos Struct 2019;214:348–58.
[9] Uhlig K, Spickenheuer A, Gliesche K, Karb I. Strength of CFRP open hole laminates made from NCF, TFP and braided preforms under cyclic tensile loading. Plastics, Rubber Compos 2010;39(6):247–55.
[10] Fial J, Harr M, Böhler P, Middendorf P. Automated wet compression moulding of load-path optimised TFP preforms with low cycle times. IOP Conf Ser Mater Sci Eng 2018;406:012018.
[11] Rihaczek G, Klammer M, Başnak O, Petrš J, Grisin B, Dahy H, et al. Curved foldable tailored fiber reinforcements for moldless customized bio-composite structures. proof of concept: Biomimetic NFRP stools. Polymers 2020;12(9):2000.
[12] Takezawa M, Otoguro Y, Matsuo K, Shibutani T, Sakurai A, Maekawa T. Fabrication of doubly-curved CFRP shell structures with control over fiber directions. Comput Aided Des 2021;136:103028.
[13] Syerko E, Comas-Cardona S, Binetruy C. Models of mechanical properties/behavior of dry fibrous materials at various scales in bending and tension: A review. Composites A 2012;43(8):1365–88.
[14] Gereke T, Döbrich O, Hübner M, Cherif C. Experimental and computational composite textile reinforcement forming: A review. Composites A 2013;46:1–10.
[15] Syerko E, Comas-Cardona S, Binetruy C. Models for shear properties/behavior of dry fibrous materials at various scales: a review. Int J Mater Form 2015;8(1):1–23.

[16] Allwood RJ, Bajarwan AA. A new method for modelling reinforcement and bond in finite element analyses of reinforced concrete. Internat J Numer Methods Engrg 1989;28(4):833–44.
[17] Cunha VM, Barros JA, Sena-Cruz JM. A finite element model with discrete embedded elements for fibre reinforced composites. Comput Struct 2012;94–95:22–33.
[18] Markou G, Papadrakakis M. An efficient generation method of embedded reinforcement in hexahedral elements for reinforced concrete simulations. Adv Eng Softw 2012;45(1):175–87.
[19] De Luycker E, Morestin F, Boisse P, Marsal D. Simulation of 3D interlock composite preforming. Compos Struct 2009;88(4):615–23.
[20] Allaoui S, Boisse P, Chatel S, Hamila N, Hivet G, Soulat D, et al. Experimental and numerical analyses of textile reinforcement forming of a tetrahedral shape. Composites A 2011;42(6):612–22.
[21] Capelle E, Ouagne P, Soulat D, Duriatti D. Complex shape forming of flax woven fabrics: Design of specific blank-holder shapes to prevent defects. Composites B 2014;62:29–36.
[22] Allaoui S, Hivet G, Soulat D, Wendling A, Ouagne P, Chatel S. Experimental preforming of highly double curved shapes with a case corner using an interlock reinforcement. Int J Mater Form 2014;7(2):155–65.
[23] Boisse P, Hamila N, Vidal-Sallé E, Dumont F. Simulation of wrinkling during textile composite reinforcement forming. influence of tensile, in-plane shear and bending stiffnesses. Compos Sci Technol 2011;71(5):683–92.
[24] Creech G, Pickett AK. Meso-modelling of non-crimp fabric composites for coupled drape and failure analysis. J Mater Sci 2006;41(20):6725–36.
[25] Bel S, Hamila N, Boisse P, Dumont F. Finite element model for NCF composite reinforcement preforming: Importance of inter-ply sliding. Composites A 2012;43(12):2269–77.
[26] Ibrahimbegović A, Frey F, Kožar I. Computational aspects of vector-like parametrization of three-dimensional finite rotations. Internat J Numer Methods Engrg 1995;38(21):3653–73.
[27] Géradin M, Cardona A. Flexible multibody dynamics: a finite element approach. New York: Wiley–Blackwell; 2001.
[28] Ritto-Corrêa M, Camotim D. On the differentiation of the rodrigues formula and its significance for the vector-like parameterization of Reissner-Simo beam theory: Differentiation of rodrigues formula. Internat J Numer Methods Engrg 2002;55(9):1005–32.
[29] d'Agostino M, Giorgio I, Greco L, Madeo A, Boisse P. Continuum and discrete models for structures including (quasi-) inextensible elasticae with a view to the design and modeling of composite reinforcements. Int J Solids Struct 2015;59:1–17.
[30] Harrison P. Modelling the forming mechanics of engineering fabrics using a mutually constrained pantographic beam and membrane mesh. Composites A 2016;81:145–57.
[31] Taylor RL, Oñate E, Ubach P-A. Finite element analysis of membrane structures. In: Oñate E, Kröplin B, editors. Textile composites and inflatable structures. Vol. 3. Berlin/Heidelberg: Springer-Verlag; 2005, p. 47–68.
[32] Carpenter NJ, Taylor RL, Katona MG. Lagrange constraints for transient finite element surface contact. Internat J Numer Methods Engrg 1991;32(1):103–28.